7th International Symposium on Hydraulic Structures Aachen, Germany, 15-18 May 2018
ISBN: 978-0-692-13277-7 DOI: 10.15142/T3XS8P

Free-Surface Instabilities in High-Velocity Air-Water Flows down Stepped Chutes

M. Kramer[1], & H. Chanson[1]
[1]*The University of Queensland, School of Civil Engineering, Brisbane QLD 4072, Australia*
E-mail: m.kramer@uq.edu.au

Abstract: *Recent advances in technology have permitted the construction of large dams and spillways. One type, the stepped spillway, is designed to spill floods over the chute with substantial regular energy losses. This article presents an experimental investigation of free-surface instabilities within the non-aerated and aerated region of a gravity-type stepped spillway (θ = 45°). Intense splashing and ejection of water droplets are characteristics of the transition flow regime and typically follow the primary breakup of the liquid phase. These formation processes might be of particular interest concerning the dimensioning of stepped chute sidewalls. The current study determines velocities of evolving liquid ligaments by means of high-speed video analysis. The video sequences are recorded within the upper transition flow sub-regime. To minimise the influence of sidewall effects, the camera is focussed on a vertical plane inside the channel. Simultaneously, unsteady water surface elevations are measured with a series of acoustic displacement meters mounted alongside the flume, perpendicular to the pseudo bottom formed by the step edges. A correlation analysis is performed on the output of the acoustic sensors in order to determine characteristic time scales of surface fluctuations as well as celerities of liquid structures next to the free-surface. The turbulent fluctuations of the free-surface increase rapidly with further distance from the inception point of self-aeration. This is likely to be associated with enhanced air entrainment and equally increased amount of air-water ejections above the aerated flow region, showing the occurrence of strong hydrodynamic fluctuations within the transition flow regime. The present investigation emphasises the feasibility of using high-speed video analysis to provide relevant flow information next to the sidewall of spillway models.*

Keywords: *Stepped spillway, free-surface instabilities, particle tracking velocimetry, acoustic displacement meters, transition flow regime.*

1. Introduction

The flow down stepped chutes within the transition and the skimming flow regime is typically characterized by two distinct regions: a non-aerated, clear-water flow region in the upper section of the stepped spillway followed by an aerated downstream region. The smooth flow in the non-aerated region usually appears glassy (Chanson, 2002) and is characterized by turbulent boundary layer growth and a clear interface between air and water. A pronounced feature of this region is the presence of free-surface disturbances which emerge from the air-water interface and grow with increasing distance from the spillway crest (Chanson, 2013). The formation of these perturbations is believed to be caused by different mechanisms, depending on turbulence quantities as well as on the relative velocities between air and water. The disturbances can be characterized as vanishing waves, capillary waves, or Kelvin-Helmholtz instabilities (Valero and Bung, 2016). In this context, it is important to understand the concept of air being transported as bubbles ("entrained air") and air transported with the flow in the roughness of the water surface ("entrapped air") (Killen, 1968; Toombes and Chanson, 2007), as it implies that the mean air concentration in the non-aerated region of the spillway is increasing as a consequence of the growth of the disturbances, as shown by Meireles et. al. (2012) and Pfister and Boes (2014).

The point separating the non-aerated and the aerated region of a spillway is broadly called the inception point of air entrainment and defines a very narrow range of flow conditions between first and continuous bubble entrapment/entrainment (Chanson, 2009). Different approaches for a phenomenological determination of the inception point location have been introduced in the past (Meireles et al., 2012), including: (1) the visual detection of the cross section where a continuous presence of air bubbles is apparent (majority of the studies, e.g., Chanson and Toombes, 2002; Relvas and Pinheiro, 2008), (2) the identification of the cross section where the mean air concentration equals $C_{mean} = 0.2$ (Bung, 2011), and (3) the detection of the cross section where the void fraction at the pseudo-bottom of the spillway equals $C = 0.01$ (Boes and Hager, 2003). It is emphasized that the visual detection incorporates the highest degree of uncertainty and may be subjective but, at the same time, allows for a simple application under field conditions. A theoretical framework for the determination of the inception point was developed within the early work of Bauer (1954), Straub and Anderson (1958), and Keller and Rastogi (1975), proposing that the aeration is taking place at the intersection of the growing boundary layer and the free-surface. Boundary layer type equations have been

widely used in the prediction of the inception point, and several empirical equations were developed, compare Cain and Wood (1981), Wood et al. (1983), Chanson (1994, 2002), Meireles et al. (2012), and Hunt and Kadavy (2013). Alternative concepts incorporate a formulation where the onset of air entrainment occurs when the turbulent shear stress close to the free-surface is larger than the resisting surface tension force per unit area (Chanson, 2009).

The flow next to the inception point is usually extremely turbulent, and sometimes the free-surface appears to be subjected to a flapping mechanism (Chamani, 2001; Chanson, 2002). Immediately downstream of the inception point, continuous entrainment of air, also called self-aeration, takes place and the flow parameters show a sudden change, e.g., an increase of void fraction and flow bulking. The flow at the inception point is usually characterized as a rapidly varied flow region (RVF) (Zhang and Chanson, 2017). Only few studies investigated the flow properties upstream and downstream of the inception point due to the fact that velocity measurements with intrusive phase-detection probes become difficult at low void fractions. Table 1 shows a summary of laboratory studies on free-surface roughness/instabilities in smooth and stepped spillway flows. Note that the study of Pfister and Hager (2011) is included as the transition from entrapment and entrainment of air is shown by means of phase-detection probe measurements.

Table 1. Studies on free-surface roughness/entrapped air in smooth and stepped spillway flows; ADM: Acoustic displacement meter, CP: Conductivity probe; FO: Fiber-optical probe; VC: High-speed video camera

Reference	Chute type	θ [°]	W [m]	q [m^2/s]	d_c/h [-]	Flow region	Instrumentation
Pfister and Hager (2011)	Stepped	50	0.5	0.11 - 0.65	1.1 - 3.8	Non-aerated Aerated	FO, VC (1,000 fps, 512×512 pix)
Meireles et al. (2012)	Stepped	53	1.0	0.05 - 0.20	1.1 - 8.0	Non-aerated	CP, Pitot-tube
Bung (2013)	Stepped	26.6	0.3	0.07 - 0.11	1.8 - 3.6	Aerated	ADM, VC (1,220 fps, 256×256 pix)
Felder (2013) Felder and Chanson (2014)	Stepped	26.6	1.0	0.116 - 0.202	1.1 - 1.6	Non-aerated Aerated	ADM, CP
Hunt et al. (2014)	Stepped	14 - 26.6	1.52 - 5.49	0.11 - 1.83	1.1 - 28.6	Non-aerated Aerated	FO, Pitot tube
Valero and Bung (2016)	Smooth	26.6	0.5	0.05 - 0.230	-	Non-aerated	ADM, Anemometer
Present study (2017)	Stepped	45	0.99	0.067	0.8	Non-aerated Aerated	ADM, VC (2,000 fps, 1280×800

In order to improve the characterization of free-surface disturbances in stepped spillway flows, acoustic displacement meter measurements were conducted within the non-aerated and the aerated region at the centerline of the chute. Furthermore, the region immediately downstream of the inception point was examined by means of high-speed video analysis and acoustic displacement meter measurements. Herein, three acoustic sensors and a video camera were synchronized, and all measurement devices captured two-phase flow parameters at a fixed distance from the channels inner sidewall. The measurements included:

1) Acoustic displacement meter measurements at the channels centerline ($2z/W = 0.0$) within the non-aerated and the aerated transition flow regime.
2) Simultaneous high-speed video and acoustic displacement meter measurements immediately downstream of the inception point of air entrainment; the measurements were conducted at a distance of 11.5 cm ($2z/W = 0.77$) from the inner sidewall.

Auto- and cross-correlation analyses were performed on the acoustic displacement meter data, and characteristic time-scales of the free-surface as well as celerities of the surface-disturbances were obtained. The recorded image sequences of the high-speed video camera were processed by means of particle tracking velocimetry (PTV). To the knowledge of the authors, the PTV method has not been applied to aerated spillway flow so far. Herein, a modified version of the toolbox PTVlab was used, and the next section presents a short introduction of this approach.

2. Methodology – Particle Tracking Velocimetry

Particle tracking velocimetry is a non-intrusive image based technique used to determine instantaneous velocities in a moving fluid. The method works in a Lagrangian frame of reference, and single particles are detected and tracked

within a series of consecutive images. The detection of the particles occurs at random locations in a defined region of interest (ROI). The velocity of these particles is derived by dividing their displacement by a known time interval, typically corresponding to the time delay of two consecutive images of the given image series.

Particle tracking velocimetry has two advantages over the standard cross-correlation particle image velocimetry (PIV), including the location of the measured velocity within the limit of the traceability of particles and the possibility of full three-dimensional measurements (Ohmi and Li, 2000). In contrast, PTV usually uses lower seeding densities and is often referred to the low-image-density mode of PIV (Adrian, 1991). A simple justification for the low-density-mode is that particle detection and tracking becomes difficult for higher densities. However, current algorithms for particle detection combined with developed algorithms to solve for the temporal matching problem have provided a good performance for images with a moderately high particle density (Brevis et al., 2011). Fundamental reviews on the methodology of particle tracking velocimetry are introduced by Maas et al. (1993) and Malik et al. (1993). The chain of data processing can be subdivided into the following steps: a) image pre-processing, b) particle detection, c) movement tracking, and d) post-processing.

Image pre-processing: It is well known that image pre-processing is beneficial to improve the results of PIV or PTV algorithms. Within the present work, a background image is calculated from the complete sequence and then subtracted from the processed image.

Particle detection: The single-value threshold (SVT) binarization was the standard approach for a long time in particle tracking velocimetry. More recent methods for identifying particle centres, e.g., the dynamic threshold-binarization method (DTB) or the particle mask correlation method (PMC) have improved the performance of PTV and shifted the application to images with higher particle densities (Ohmi and Li, 2000). The Particle mask correlation proposed by Takehara end Etoh (1999) was used in this study. Herein, a brightness pattern of a particle image is referred to as a particle mask and scanned over the entire image plane. This brightness pattern is approximated as a centred peak with concentrically decreasing brightness, defined in terms of a two-dimensional Gaussian distribution:

$$I(x,y) = M \times \exp\left[-\frac{(x - x_C)^2 + (y - y_C)^2}{2\sigma^2} \right] \quad (1)$$

where I(x,y) is the brightness value, M is the peak brightness, x_C and y_C are the coordinates of the particles image centre, and σ is the standard deviation, referring to the radius of the particle image. Small subareas with high correlation coefficients are indicated as particle centroids by calculating cross-correlation coefficients on each pixel location. To increase the accuracy of the particle tracking, a subpixel estimator using a Gaussian 3-point fit (Nobach and Honkanen, 2005) was implemented by the authors.

Movement tracking and post-processing: The first approaches for tracking the movement of detected particles in consecutive image planes are the multi frame tracking method (Hassan and Canaan, 1991) and the binary-image cross-correlation method (Uemura et al., 1989; Hassan et al., 1992). In the present study, a modified cross-correlation algorithm developed by Brevis et al. (2011) was applied. The algorithm makes use of the particle distributions patterns, and the velocity associated with a particle is found by using the highest cross-correlation coefficient obtained after comparing the reference distribution in the first frame and a set of sub-matrices in the second frame (Brevis et al., 2011). The obtained data were post-processed by using a two-frame forward search algorithm, which discards particles that are not detected over three consecutive frames.

3. Experimental Setup and Instrumentation

3.1. Stepped Spillway Facility

Experimental investigations were conducted on a relatively large-size model of a steep ($\theta = 45°$) stepped spillway (Fig. 1). The physical model of the stepped spillway consisted of broad-crested weir inlet followed by a 12.4 m long and 0.985 m wide channel. The channel ended with a free overfall into a recirculation sump and the model had an independent open water circuit. The water recirculation was adjusted by three centrifugal pumps, operating at variable rotational speed. The spillway consisted of 12 steps with a step length of $l = 0.1$ m and a step height of $h = 0.1$ m. The width of the steps corresponded to the channel width of $W = 0.985$ m, and the steps were made of water-sealed plywood. The step edges were increasingly numbered, where step edge 0 corresponds to the rounded downstream

edge of the broad crested weir, see Fig. 1. For further information concerning, e.g., the inlet basin or the broad crested weir, see Zhang and Chanson (2016) and Kramer and Chanson (2018).

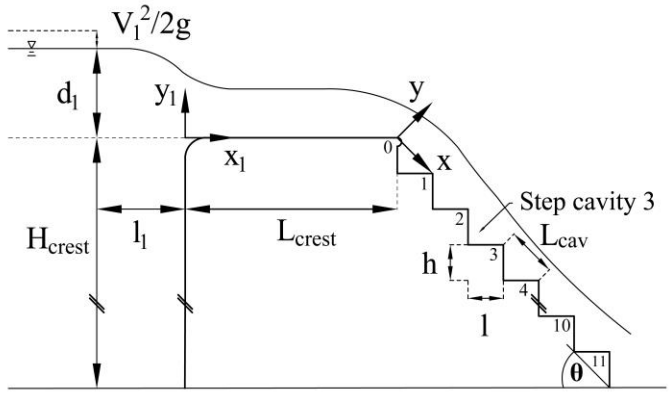

Figure 1. Definition sketch of the stepped spillway and the broad crested weir; sketch according to Kramer and Chanson (2018)

3.2. Instrumentation

The clear-water flow depths at the middle of the weir crest and in the upstream section of the spillway were measured with point gauges located at the channel centreline. The longitudinal locations of the point gauges were at x_1/L_{crest} = -0.92 and x_1/L_{crest} = 0.5; the accuracy of the point gauges was within ±1 mm in the clear-water region. Unsteady water surface elevations were recorded with a series of three acoustic displacement meters mounted along the channel and perpendicular to the pseudo bottom formed by the step edges. The sensors of the type Microsonic™ Mic+25/IU/TC were attached to a trolley (centreline measurements, setup not shown) and to a slide rail of the channel, see Fig. 2B. The sensors were equipped with cylindrical extensions of 4 cm length (see Appendix). The purpose of these extensions was to avoid splashing onto the sensors and to narrow the detection area. The extensions also minimized the interference of adjacent sensor signals due to the exceedance of recommended assembly distances. The measurement distance of the implemented Microsonic™ Mic+25/IU/TC sensors ranged from 30 mm to 350 mm with ±1 % accuracy and 32 m/s response time.

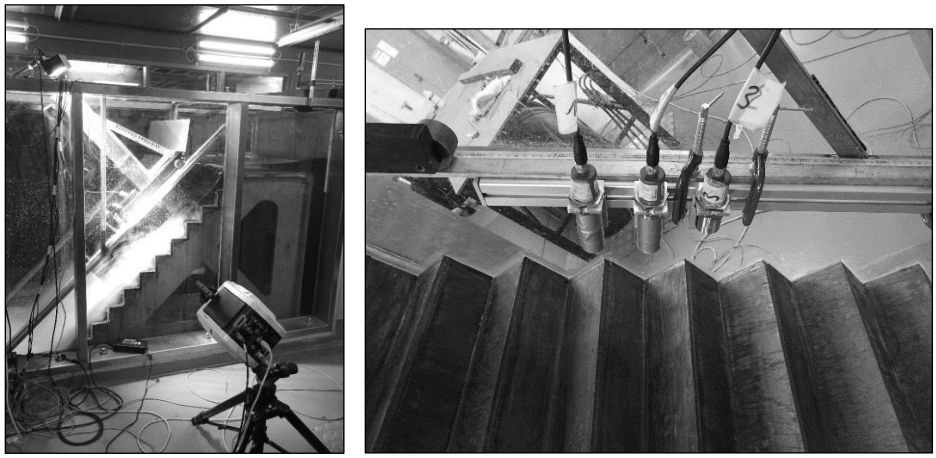

Figure 2. Photographs of the experimental setup
(A, left): Orientation of the high-speed video camera in front of the stepped spillway; d_c/h = 0.8; Re = 2.7×10^5
(B, right): Mounting of the acoustic displacement sensors alongside the spillway channel; 2z/W = 0.77; flow direction from left to right

The acoustic sensors were synchronised with the high-speed video camera, and the sensor signals were scanned at frequencies of 100 Hz for durations up to 300 s. Note that the sample rate of the acoustic displacement sensors was limited by their response time. Erroneous spikes in the sensor signals were removed by threshold techniques and replaced by linear interpolation (compare Appendix).

Air-water flow properties were recorded with a Phantom v2011 high-speed video camera. The camera was equipped with an AF Nikkor 50 mm f/1.4 lens, capable of generating images with a relatively small degree of distortion. Figure 2A shows a typical camera arrangement in front of the physical model. The camera was inclined at an angle of 45° and aligned with the pseudo bottom of the stepped spillway. The distance between camera lens and sidewall was 1.0 m. The camera was focused on a vertical plane parallel to the sidewall and cutting the beams of the acoustic displacement meters. Images were recorded at a frame rate of 2,000 fps with a resolution of 1280×800 pixels. In order to achieve a shallow depth of field, the aperture opening of the camera was set to f/1.4. The flow was illuminated with a 4×6 high intensity LED matrix attached to the sidewall of the channel. To enhance the contrast and to mask abundant information in the transversal dimension, the backside of the channel was covered with cloth and a black sprayed wooden board was mounted within the channel at a location of 2z/W = 0.7, next to the free-surface of the flow. Checks ensured that the mounted board was not disturbing the flow. The synchronisation of the camera was done by hardware triggering.

3.3. Investigated Flow Conditions

The experiments were conducted for a discharge of $d_c/h = 0.8$ within the upper transition flow regime TRA2, as defined in Chanson and Toombes (2004). Table 2 summarises the experimental flow conditions. Herein, L_i indicates the longitudinal position of the inception point of air entrainment, identified by visual detection, measured from step edge 0 (Fig. 1).

Table 2. Experimental flow conditions of the present study

d_c/h	q [m^2/s]	θ [°]	W [m]	Regime	L_i/L_{cav}	Re
0.8	0.068	45	0.985	TRA2	2.0	2.7×10^5

4. Experimental Results (1): Acoustic Displacement Meter Measurements

4.1. Free-Surface Elevation and Turbulent Fluctuations

Visual observations of the free-surface upstream of the inception point showed an undulating surface with a wave length of approximately twice the cavity length at $d_c/h = 0.8$. The largest amplitude of the free-surface waves was found above the first step, decreasing towards the free-surface inception point. In this context, it is emphasizsed that the wave length of the surface undulations in the non-aerated region is dependent on the flow rate. A wave length in the order of a single cavity length is expected at lower discharges. This pattern was observed by Chanson (2002) and can simply be justified by the fact that step edges act as flow singularities, introducing disturbances at a length scale equivalent to the cavity length.

Fig. 3 shows the time averaged depth profiles as combined results of the acoustic displacement meter experiments, including the location of the inception point (vertical dashed line) and characteristic flow depths of intrusive phase-detection probe measurements (centreline) from an earlier study by Kramer and Chanson (2018). Herein, d is the equivalent clear water depth defined as:

$$d = \int_{y=0}^{Y_{90}} (1-C) \times dy \tag{2}$$

where C is the void fraction and Y_{90} is the characteristic air-water depth where the void fraction equals C = 0.9. The recorded mean surface profiles at the centreline and next to the sidewall were in good agreement and showed a rapidly varied flow region and flow bulking immediately downstream of the inception point of air entrainment. Flow bulking is a common feature in stepped spillway flows (Chanson, 1995, 2002; Matos, 2000; Meireles et al., 2014) and spanned in the current investigation over approximately 4 step cavity lengths downstream of the self-aeration point. This was in accordance with earlier observations by Zhang and Chanson (2017).

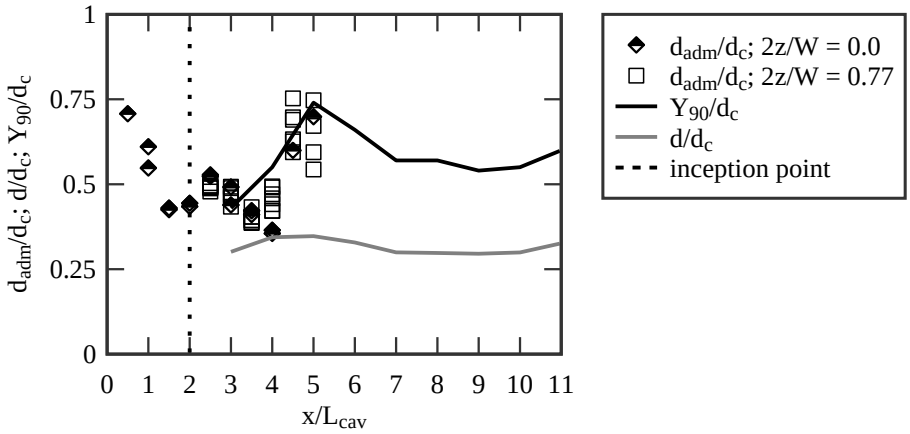

Figure 3. Dimensionless free-surface characteristics – comparison with intrusive phase-detection probe measurements of the characteristic air-water depth Y_{90} and equivalent clear water depth d (Eq. 2); $d_c/h = 0.8$; $\theta = 45°$

The measured free-surface elevation data were subject to rapid fluctuations at the different positions along the stepped chute. These fluctuations were quantified in terms of the standard deviations d'_{adm}. Fig. 4A shows the dimensionless standard deviations d'_{adm}/d_c normalised by the inception point location including data from Felder (2013). The fluctuations of the free-surface were within $0.06 < d'_{adm}/d_c < 0.39$, increasing rapidly with further distance from the inception point. This was associated with enhanced air entrainment and an increased amount of air-water ejections above the aerated flow region. Visual observations showed rapidly growing surface disturbances and increased droplet ejections immediately downstream of the inception point. The present findings are consistent with previous experiments by Felder (2013), undertaken within the skimming flow region on a non-uniform stepped spillway with a slope of $\theta = 26.6°$. Felder (2013) measured surface fluctuations at the centreline for three different discharges in a range of about $0.025 < d'_{adm}/d_c < 0.075$ (non-aerated region) and $0.06 < d'_{adm}/d_c < 0.23$ (aerated region). The data of the present study show a good agreement in terms of the fluctuations in the non-aerated region and at the inception point. With further distance to the inception point location, the current measurements indicated a higher magnitude of fluctuations. Possible reasons include the nature of the investigated transition flow regime, characterised by strong hydrodynamic fluctuations. The integral auto-correlation integral time scales provided a description of the longitudinal flow structure and were calculated as:

$$T_{xx} = \int_{\tau=0}^{\tau=\tau(R_{xx}=0)} R_{xx}(\tau) \times d\tau \quad (3)$$

where T_{xx} is the auto-correlation integral time scale, τ is the time lag, and R_{xx} is the normalised auto-correlation function. Note that filtered data of the acoustic sensors were divided into sub-segments of 30 s duration, and the integration of the auto-correlation functions was performed until the first crossing of the abscissa. Further details concerning the used filtering technique are given in the Appendix.

Figure 4B shows a comparison of the longitudinal auto-correlation time scales of free surface fluctuations. The time scales herein were in a range between $0.014 \text{ s} < T_{xx} < 0.51 \text{ s}$, showing a decrease with further distance from the weir crest. This characteristic is believed to be related to the accelerating flow and the growth of surface disturbances. Due to strong surface fluctuations at the inception point, a larger data scattering is observed around this location (e.g., flapping mechanism). In this context, measurement instrumentation with a higher sampling frequency and a smaller detection area would be beneficial for future investigations of free-surface fluctuations and integral time scales. The auto-correlation time scales observed by Felder (2013) were in a range between $0.05 \text{ s} < T_{xx} < 0.9 \text{ s}$ and are in good agreement within the non-aerated region. The deviations in the aerated region remained unclear.

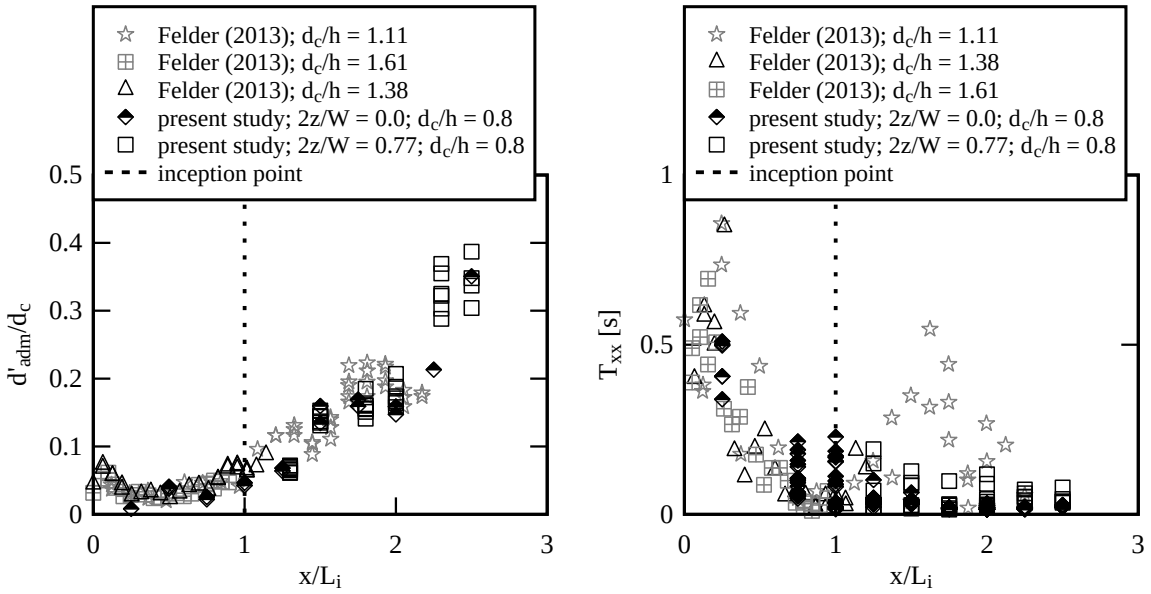

Figure 4. Longitudinal free surface characteristics obtained with acoustic displacement meters
(A, left) Dimensionless free-surface fluctuations d'_{adm}/d_c normalised by the inception point location
(B, right) Auto-correlation time scales of free-surface fluctuations in transition and skimming flows

4.2. Auto- and Cross-Correlation Analyses

The acoustic sensors detected the free-surface elevation at adjacent longitudinal positions, and the signals were processed by means of auto- and cross-correlation analyses. Figure 5 shows representative correlation functions for the acoustic sensors next to the sidewall at longitudinal positions of x/L_{cav} = 2.5, 3.0, and 3.5 (Fig. 5A) and x/L_{cav} = 4.0 and 4.5 (Fig. 5B). For clarity, the time lag of maximum cross-correlation coefficient is indicated in both figures. The shape of the cross-correlation functions exhibits a clear broadening when compared to the auto-correlation functions, and the correlation coefficients diminish noteworthy in longitudinal direction, reflecting the loss of information with increasing longitudinal distance. Further conclusions can be drawn by comparing the time lags of the cross-correlation functions at different locations. The time lag of the cross-correlation function between x/L_{cav} = 4.0 and 4.5 was slightly smaller than the time lag of the function between x/L_{cav} = 2.5 and 3.0, representing an acceleration of free-surface structures within the investigated flow region.

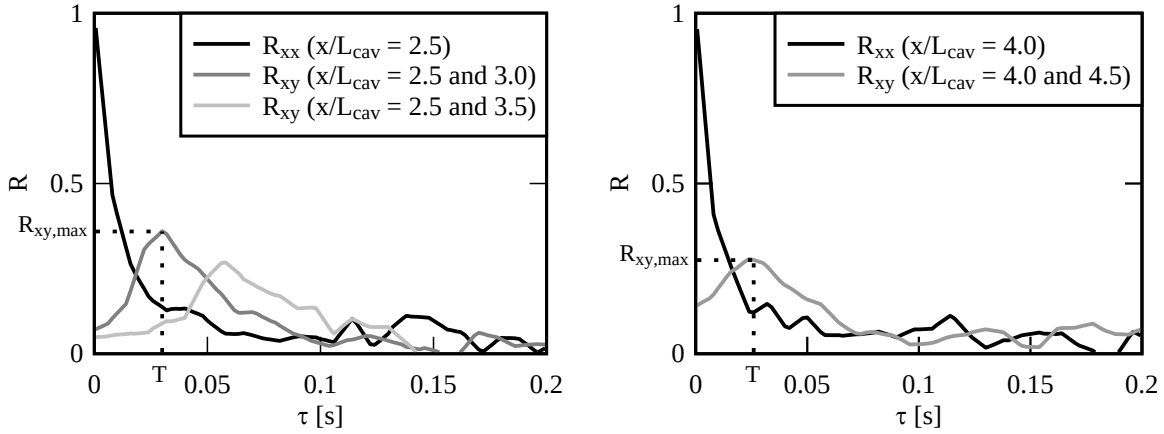

Figure 5. Representative auto- and cross-correlation functions between different acoustic sensors above the aerated transition flow region; 2z/W = 0.77; d_c/h = 0.8; θ = 45°
(A, left) x/L_{cav} = 2.5, 3.0 and 3.5
(B, right) x/L_{cav} = 4.0 and 4.5

Furthermore, the maximum correlation coefficient of the function between x/L_{cav} = 4.0 and 4.5 was lower than the coefficient of the function between x/L_{cav} = 2.5 and 3.0. This was interpreted as an increase of randomness in the longitudinal direction of the aerated flow region. The correlation analysis allowed for a determination of the celerity of liquid surface instabilities by involving the time lag and the longitudinal separation of the sensors. The celerity was calculated with $C_{adm} = \Delta x / T$, where C_{adm} is the celerity, Δx is the longitudinal distance between two adjacent acoustic displacement meters and T is the time lag for which the cross-correlation function reached a maximum (see Fig. 5). The time lag corresponded to the travel time of the surface instabilities between two sensor positions and the longitudinal distance between the sensors was $\Delta x = \sqrt{2} / 2 \times 0.1$ m. The celerities of the free-surface disturbances were in a range between C_{adm} = 2.36 m/s and 2.98 m/s and are presented in the next section, together with the particle tracking velocimetry results.

5. Experimental Results (2): Particle Tracking Velocimetry

Velocities of disturbances evolving from the air-water interface were determined based on the particle tracking velocimetry method described in Section 2. It is believed that the PTV method has advantages in estimating velocities next to the free-surface due to its Lagrangian approach when compared to other image based velocimetry methods. It is well documented that, e.g., the bubble image velocimetry (BIV) or the optical flow method (OF) tend to underestimate flow velocities in regions with high void fractions (Bung, 2011; Valero and Bung, 2016). Within the current investigation, a video sequence with a sample duration of 8.3 s and a sampling rate of 2,000 Hz was examined. Two regions of interest next to the free-surface were defined, covering a longitudinal distance from x/L_{cav} = 2.5 to 3.5. Fig. 6B shows a representative image of the defined regions and an evolving free-surface disturbance next to the inception point of air entrainment at L_i/L_{cav} = 2.0. Detected particles are marked as dark circles and instantaneous velocities are plotted as vectors. It is pointed out that the detected particles corresponded to textures and brightness spots on the surface disturbance rather than to particles in a stricter sense. A time- and spatial-averaged velocity was subsequently calculated for both regions in order to compare the performance of the PTV algorithm with the measurements of the acoustic sensors and the phase-detection probe. Fig. 6A presents a comparison of the calculated streamwise velocities as function of x/L_{cav}.

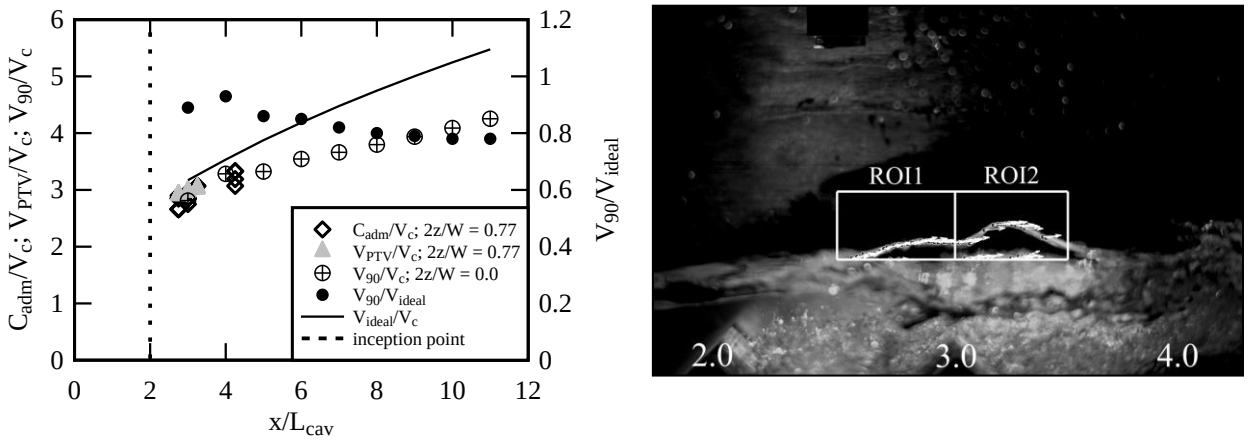

Figure 6. Particle tracking within the upper region of the transition flow regime downstream of the inception point; d_c/h = 0.8; (A, left) Streamwise velocities of free-surface disturbances in the aerated region of the transition flow regime; (B, right) Regions of interest (ROI), detected particles and instantaneous velocities (plotted as vectors); flow direction from left to right; camera focused on a vertical plane at 2z/W = 0.77

Herein, C_{adm} is the celerity determined by the cross-correlation analysis of the acoustic displacement meters, V_{PTV} is the velocity obtained by the particle tracking velocimetry method, V_{90} is the velocity measured with an intrusive phase-detection probe at a location where C = 0.9 (Kramer and Chanson, 2018), V_c is the critical velocity defined as $V_c = \sqrt{g \times d_c}$, and V_{ideal} is the ideal fluid velocity, deducted from the one-dimensional steady flow energy equation:

$$V_{ideal} = \sqrt{2g(H_1 - z - d \times \cos\theta)} \quad (4)$$

where V_{ideal} is the ideal velocity, H_1 is the upstream total head, θ is the channel slope, d is the flow depth, and z is the bed elevation. In line with the theory, the dimensionless velocities increased with increasing distance from the downstream edge of the broad crested weir. Overall, a good agreement of the velocity data was observed and all three measurement methods were found to be suitable for determining velocities within the upper region of the aerated transition flow. It is worthwhile to mention that the particle tracking velocimetry allowed for a correct velocity determination even in regions with high void fractions. A comparison of interfacial velocities V_{90} with the ideal fluid theory shows that the velocities were in a range of 0.8 to 0.95 of the ideal velocity. This is physically correct as the ideal velocities are not accounting for friction losses.

6. Conclusion

The present study investigated free-surface instabilities within the upper transition flow regime of a steep ($\theta = 45°$) stepped spillway. Free-surface elevations and fluctuations were recorded in the aerated and the non-aerated flow region by means of acoustic displacement meter measurements. The free-surface profile indicated flow bulking and a rapidly varied flow region next to the inception point of self-aeration. The fluctuations compared well with earlier skimming flow data and the surface-instabilities showed a growth in longitudinal direction of the chute. Visual observations highlighted droplet ejection and intense splashing associated with growing instabilities downstream of the inception point.

Velocities within the upper flow region where determined by means of cross-correlation analysis (acoustic signals) and particle tracking velocimetry. The video camera was synchronized with the acoustic displacement meters and was focused on a vertical plane parallel to the sidewall of the channel. The focal plane was cutting the beams of the acoustic sensors at a distance of 11.5 cm from the inner sidewall, allowing for a direct data comparison between the different flow measurement systems. It was found that the velocities of the tracked particles were in good agreement with the results of the cross-correlation analysis and earlier phase-detection probe measurements. This is remarkable as other image-based velocimetry approaches tend to underestimate velocities in regions with high void fractions close to the free-surface. Overall, the current investigation improves the characterisation of high-velocity air-water flows down stepped chutes and emphasises the feasibility of using particle tracking methods to provide relevant flow information next to the sidewall of hydraulic models.

7. Acknowledgments

The authors acknowledge the fruitful discussions with Daniel Valero (FH Aachen) and the technical assistance of Jason Van Der Gevel and Stewart Matthews (The University of Queensland). Matthias Kramer was supported by DFG grant KR 4872/2-1.

8. Appendix - Calibration of Acoustic Displacement Sensors

The acoustic displacement sensors were calibrated on-site by placing wooden boards with different thicknesses parallel to the pseudo bottom of the spillway. During calibration, the sensors were sampled at 100 Hz for duration of 30 s and a linear relationship between the voltage output and the distance from the sensor head was obtained for each sensor. Fig. 7A shows calibration curves for the three sensors and standard calibration, represented by the black dashed line. At standard calibration, sensor signals of 0 V and 10 V correspond to distances between sensor head and surface of 30 mm and 350 mm.

To determine whether the cylindrical extensions had an influence on the functionality of the acoustic surface detection, an acoustic sensor (with and without extension) was mounted on a horizontal bar, facing a flat and white surface. The sensor signals were recorded for both configurations at a sample rate of 100 Hz for a duration 30 s. Fig. 7B shows the raw signals of the conducted measurements. These signals included some erroneous spikes, appearing for both configurations. The probability mass functions, mean values and standard deviations of the signals are given in Fig. 7C. The statistical parameters of the signals were in good agreement for both sensor configurations. It was concluded that the cylindrical extensions had a negligible influence on the free surface measurements with the acoustic displacement meters. During operation of the spillway model, the raw outputs of acoustic displacement meter sometimes included errors. These errors can have various causes, including the following (Wang and Chanson, 2013):

a) Acoustic beam fails to be captured by the sensor because of some angle of the water surface,
b) Acoustic beam is reflected by a splashing droplet or a water drop stuck at the sensor head, and
c) Interference by adjacent sensors.

The errors resulting from interference of adjacent sensors and from water drops stuck at the sensor heads were reduced by the implemented circular extensions. However, due to the mentioned causes, erroneous spikes departing from the major signal distribution were still observed in the sensor output. These erroneous spikes were removed by a threshold corresponding to the mean value ± 3 times the standard deviation of the raw signal (compare Bung, 2013). The affected points were replaced by linear interpolation and signals with more than 20% of filtered data were excluded from the post-processing. The statistical data analyses were conducted on the signals after removal of erroneous data.

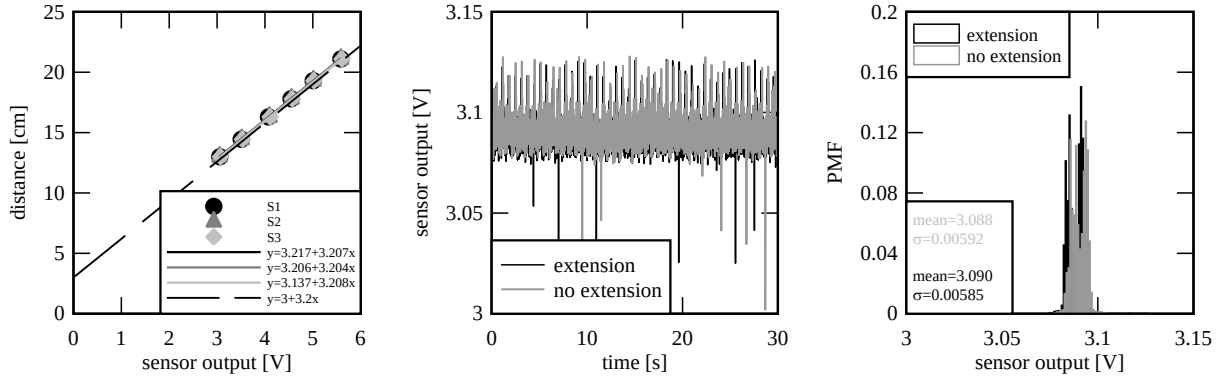

Figure 7. Calibration curves and signal comparison for both sensor configurations
(A, left) Calibration curves for the acoustic displacement meters
(B, middle) Raw signals of the acoustic displacement sensor – both configurations
(C, right) Probability mass functions, mean values and standard deviations

9. References

Adrian, R.J. (1991). "Particle-Imaging Techniques for Experimental Fluid Mechanics." *Annu. Rev. Fluid. Mech.,* 23, 261-304.

Bauer, W.J. (1954). "Turbulent boundary layer on steep slopes." *Trans. Am. Soc. Civil Eng*. 119 (1), 1212–1233.

Boes, R.M., and Hager, W. H. (2003). "Two phase flow characteristics of stepped spillways." *J. Hydraul. Eng*., 129(9), 661–670.

Brevis, W., Nino, Y., and Jirka, G.H. (2011). "Integrating cross-correlation and relaxation algorithms for particle tracking velocimetry." *Exp. Fluids,* 50, 135-147.

Bung, D.B. (2011). "Developing flow in skimming flow regime on embankment stepped spillways." *J. Hydraul. Res*., 49(5), 639–648.

Bung, D.B. (2013). "Non-intrusive detection of air–water surface roughness in self-aerated chute flows." *J. Hydraul. Res*., 51 (3), 322–329.

Cain, P., and Wood, I.R. (1981). "Measurements of self-aerated flow on a spillway." *J. Hydraul. Div.*, 107 (11), 1425–1444.

Chamani, M.R. (2000). "Air Inception in Skimming Flow Regime over Stepped Spillways." *Intl. Workshop on Hydraulics of Stepped Spillways*, Zürich, Switzerland, H.E. Minor & W.H. Hager Editors, Balkema Publ., 61-67.

Chanson, H. (1994). "Hydraulics of skimming flows over stepped channels and spillways." *J. Hydraul. Res.*, 32, 445-460.

Chanson, H. (1995). "Hydraulic Design of Stepped Cascades, Channels, Weirs and Spillways." Pergamon, Oxford, UK, Jan., 292 pages

Chanson, H. (2002). "The Hydraulics of Stepped Chutes and Spillways." Balkema, Lisse, the Netherlands.

Chanson, H. and Toombes, L. (2004). "Hydraulics of stepped chutes: the transition flow." *J. Hydraul. Eng.,* 41(1), 43-54.

Chanson, H., and Toombes, L. (2002). "Experimental investigations of air entrainment in transition and skimming flows down a stepped chute." *Can. J. Civ. Eng*., 29(1), 145–156.

Chanson, H. (2009). "Turbulent air–water flows in hydraulic structures: dynamic similarity and scale effects." *Environ. Fluid Mech.,* 9, 125-142.

Chanson, H. (2013). "Interactions between a Developing Boundary Layer and the Free-Surface on a Stepped Spillway: Hinze Dam Spillway Operation in January 2013." *Proc. 8th International Conference on Multiphase Flow ICMF 2013*, Jeju, Korea, 26-31 May, Gallery Session ICMF2013-005 (2:15).

Felder, S. (2013). "Air-water flow properties on stepped spillways for embankment dams: aeration, energy dissipation and turbulence on uniform, non-uniform and pooled stepped chutes." Dissertation, University of Queensland, School of Civil Engineering.

Felder, S., and Chanson, H. (2014). "Air–water Flows and Free-surface Profiles on a Non-uniform Stepped Chute." *J. Hydraul. Res.,* IAHR, 52(2), 253-263.

Hassan, Y.A. and Canaan, R.E. (1991). "Full-field bubbly flow velocity measurements using multiframe particle tracking technique." *Exp. Fluids*, 12, 49-60.

Hassan, Y.A., Blanchat, T.K. and Seeley JR, C.H. (1992). "PIV flow visualization using particle tracking techniques." *Meas. Sci. Technol.,* No. 3, pp. 633-642.

Hunt, S.L., and Kadavy, K. C. (2013). Inception point for embankment dam stepped spillways. *J. Hydraul. Eng*., 139(1):60-64.

Hunt, S.L., Kadavy, K.C., and Hanson, G.J. (2014). Simplistic design methods for moderate-sloped stepped chutes. *J. Hydraul. Eng*., 140(12):04014062-1-15.

Keller, R.J., and Rastogi, A.K. (1975). "Prediction of Flow Development on Spillways." *Jl of Hyd. Div.*, ASCE, 101(HY9), 1171-1184.

Killen, J.M. (1968). "The Surface Characteristics of Self-Aerated Flow in Steep Channels." *Ph.D. thesis*, University of Minnesota, Minneapolis, USA.

Kramer, M. and Chanson, H. (2018) "Transition flow regime on stepped spillways: Air-water flow characteristics and step-cavity fluctuations." *Environ. Fluid Mech.,* (DOI: 10.1007/s10652-018-9575-y).

Maas, G.H., Gruen, A. and Papantoniou, D.A (1993). "Particle tracking velocimetry in three-dimensional flows - Part 1: Photogrammetric determination of particle coordinates." *Exp. Fluids*, 15, 133-146.

Malik, N.A., Dracos, T. and Papantoniou, D.A. (1993). "Particle tracking velocimetry in three-dimensional flows – Part 2: Particle tracking." *Exp. Fluids*, Vol. 15, pp. 279-294.

Matos, J. (2000). "Hydraulic Design of Stepped Spillways over RCC Dams." *Intl. Workshop on Hydraulics of Stepped Spillways*, Zürich, Switzerland, H.E. Minor & W.H. Hager Editors, Balkema Publ., pp. 187-194.

Meireles, I., Renna, F., Matos, J., Bombardelli, F. (2012). "Skimming, nonaerated flow on stepped spillways over roller compacted concrete dams." *J. Hydraul. Eng.,* 138 (10), 870–877.

Meireles, I.C., Bombardelli, F.A., Matos, J., (2014). "Air entrainment onset in skimming flows on steep stepped spillways: an analysis." *J. Hydraul. Res*. 52 (3), 375–385.

Nobach, H., and Honkanen, M. (2005). "Two-dimensional Gaussian regression for sub-pixel displacement estimation in particle image velocimetry or particle position estimation in particle tracking velocimetry." *Exp. Fluids*, 38, 511-515.

Ohmi, K. and Li, H.-Y. (2000). "Particle-tracking velocimetry with new algorithms." *Meas. Sci. Technol.,* 11, 603-613.

Pfister, M., and Hager, W.H. (2011). "Self-entrainment of air on stepped spillways." *Int. J. Multiph. Flow*, 37 (2), 99–107.

Pfister, M. and Boes, R., (2014). "Discussion of "Skimming, Nonaerated Flow on Stepped Spillways over Roller Compacted Concrete Dams." by Inês Meireles, Floriana Renna, Jorge Matos, and Fabián Bombardelli."*J. Hydraul. Eng.,* 140(10).

Relvas, A.T., and Pinheiro, A.N. (2008). "Inception point and air concentration in flows on stepped chutes lined with wedge-shaped concrete blocks." *J. Hydraul. Eng*., 134(8), 1042–1051.

Straub, L.G., and Anderson, A.G. (1958). "Experiments on self-aerated flow in open channels." *J. Hydraul. Div*., 84 (7), 1–35.

Takehara, K., and Etoh, T. (1999). "A study on particle identification in PTV – particle mask correlation method." *J. Vis.*, 1(3), 313–323.

Toombes, L., and Chanson, H. (2007). "Surface Waves and Roughness in Self-Aerated Supercritical Flow." *Environ. Fluid Mech.*, 7(3), 259-270.

Uemura T., Yamamoto F., Ohmi K. (1989). "A high-speed algorithm of image analysis for real time measurement of a two-dimensional velocity distribution." Flow visualization, ASME FED-85, 129–134.

Valero, D., and Bung. D.B. (2016). "Development of the interfacial air layer in the non-aerated region of high-velocity spillway flows. Instability growth, entrapped air and influence on the self-aeration onset." *Int. J. Multiph. Flow*, 84, 66-74.

Wang, H., and Chanson, H. (2013). "Free-surface deformation and two-phase flow measurements in hydraulic jumps." Technical report, University of Queensland, School of Civil Engineering.

Wood, I.R., Ackers, P., Loveless, J. (1983). "General method for critical point on spillways." *J. Hydraul. Eng.* 109 (2), 308–312.

Zhang, G. and Chanson, H. (2016). "Hydraulics of the developing flow region of stepped spillways. I: physical modelling and boundary layer development." *J. Hydraul. Eng., 142(7).*

Zhang, G. and Chanson, H. (2017). "Self-aeration in the rapidly- and gradually-varying flow regions of steep smooth and stepped spillways." *Environ. Fluid Mech.*, 17, 27-46.